

Dense Continuous-Time Optical Flow from Events and Frames

Mathias Gehrig, Manasi Muglikar, and Davide Scaramuzza

Dept. of Informatics, Univ. of Zurich and
Dept. of Neuroinformatics, Univ. of Zurich and ETH Zurich
{mgehrig,muglikar,sdavide}@ifi.uzh.ch

Abstract. We present a method for estimating dense continuous-time optical flow. Traditional dense optical flow methods compute the pixel displacement between two images. Due to missing information, these approaches cannot recover the pixel trajectories in the blind time between two images. In this work, we show that it is possible to compute per-pixel, continuous-time optical flow by additionally using events from an event camera. Events provide temporally fine-grained information about movement in image space due to their asynchronous nature and microsecond response time. We leverage these benefits to predict pixel trajectories densely in continuous-time via parameterized Bézier curves. To achieve this, we introduce multiple innovations to build a neural network with strong inductive biases for this task: First, we build multiple sequential correlation volumes in time using event data. Second, we use Bézier curves to index these correlation volumes at multiple timestamps along the trajectory. Third, we use the retrieved correlation to update the Bézier curve representations iteratively. Our method can optionally include image pairs to boost performance further. The proposed approach outperforms existing image-based and event-based methods by 11.5 % lower EPE on DSEC-Flow. Finally, we introduce a novel synthetic dataset MultiFlow for pixel trajectory regression on which our method is currently the only successful approach.

Keywords: Event Cameras, Optical Flow, Non-linear Flow

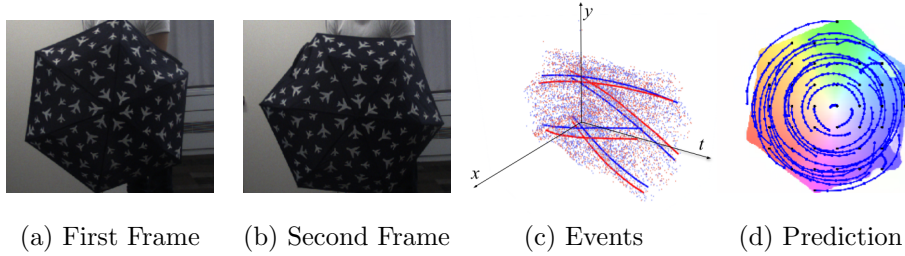


Fig. 1. Our method, trained only on simulated events, predicts dense pixel trajectories in continuous-time on real sequences.

1 Introduction

Optical flow estimation is a fundamental low-level vision task that informs about motion in pixel space. It has numerous practical applications in computational photography and videography, video compression, inverse graphics, object tracking, and robotics.

The majority of previous work addresses this problem by finding dense correspondences between two images. However, applications that use optical flow often rely on linear motion models. For example, temporal image synthesis tasks in dynamic scenes, such as frame interpolation or dynamic view synthesis [32,25], tend to rely on such assumptions. If the frame-rate is very high, such a linear motion model can be reasonable, but it breaks down if long-range correspondences are sought [45,46] or if the camera device is not capable of capturing high fps video due to storage or power consumption constraints [42]. On top of this, estimating pixel motion in the wild must deal with occlusions and objects leaving the camera field of view. Modern optical flow methods [21] attempt to address partially occluded objects but still completely fail if an independent object is only visible in one of the two frames (see Figure 6).

To address all of these challenges at once we use event cameras. In contrast to frame-based sensors, which capture images at regular intervals, event cameras register per-pixel brightness changes asynchronously and at very high temporal resolution (microseconds). Additionally, they are robust to motion blur and have a very high dynamic range [10]. For a survey on event cameras, we refer to Gallego et al. [10]. All these advantageous features make them very attractive for optical flow estimation. This has inspired prior work to propose methods to predict pixel displacements similar to two-frame optical flow [53,14]. However, event cameras provide visual cues in continuous-time, which means that predicting discrete pixel displacements ignores much of the device’s potential. With our method, we propose to close this gap with the following methodological innovations:

- Instead of predicting pixel displacements, we generalize this concept and estimate control points of Bézier curves for each pixel. As a result, our method can regress the trajectory of each pixel at arbitrary times. It also enables the second innovation:
- We use multiple correlation volumes in time to search for pixel correspondences. We then use the estimated Bézier curves to retrieve correlation features of all correlation volumes simultaneously. This enables the incorporation of motion prior and facilitates the task of finding accurate pixel trajectories.
- The use of image data is optional. We show that our approach can also work purely with event data and enable dense, pixel-wise trajectories. Furthermore, we show that a combination of image and event data outperforms single-modality approaches on both real and synthetic datasets.

The full evaluation of our method is currently not possible with existing public datasets. To the best of our knowledge, there is no dataset with moving objects

and accurate ground truth for pixel trajectories from a single reference view. Furthermore, we also require both event and image data which is by itself a rare combination. Therefore, we propose a new dataset inspired by the FlyingChairs dataset [8] that fulfills the aforementioned specifications. The overall dataset consists of approximately 10000 training and 2000 test sequences with moving objects undergoing similarity transformations in continuous-time. We use this dataset to quantitatively evaluate our method and to show promising sim2real transfer performance. Finally, we provide quantitative experiments on DSEC-Flow [14], a real-world dataset featuring a multi-camera setup consisting of event and global shutter cameras with ground truth pixel displacement maps.

2 Related Work

2.1 Optical Flow

For conciseness, we focus mostly on neural-network-based (NN-based) methods.

Image-based The vast majority of neural network-based optical flow method considers the task of estimating dense pixel displacements from a pair of frames [41,44,40,16,22,43,9,2,49,18,50,51,8]. A common component of many highly successful methods are explicit correlation volumes that guide the matching process. This inductive bias enables high performance and data efficiency [41] as well as strong cross-dataset generalization [49].

Multi-Frame optical flow estimation has been mostly explored in the self-supervised learning setting [15,19,28] or optimization-based literature [20,37,11]. Some NN-based approaches use an additional pair of frames to initialize the optical flow prediction [41] or use warped flow as input [36] to a second stage. From these multi-frame approaches, Slow Flow [20] is conceptually most related. Slow Flow estimates optical flow $\mathbf{F}_{1 \rightarrow N}$ given a sequence of N images at high frame rate (1000 fps) with dense tracking using an optimization-based approach. However, it requires a high-speed camera and complex occlusion handling that incurs a trade-off between drift and accurate prediction at motion boundaries.

Event-based Event-based optical flow algorithms can be categorized into four categories: (i) Asynchronous methods [5,12] using the Lucas-Kanade algorithm [27]. (ii) Plane fitting-based methods that exploit the local plane-like shape of spatio-temporal event streams [6,30]. (iii) Variational optimization-based approaches [4,33] that incorporate image data[33] or simultaneously estimate image intensity [4]. (iv) Learning-based approaches, most of which are trained via self-supervision [53,54,24,34,47]. Supervision is provided either by images[53,54,24] or events[34,47]. Our approach is related to E-RAFT [14], which adapts the RAFT [41] framework to event data to leverage correlation features from cost volumes to estimate dense pixel correspondences for large displacements. In contrast to E-RAFT or RAFT, we predict pixel trajectories using multiple views while we also show the advantages of combining events and frames.

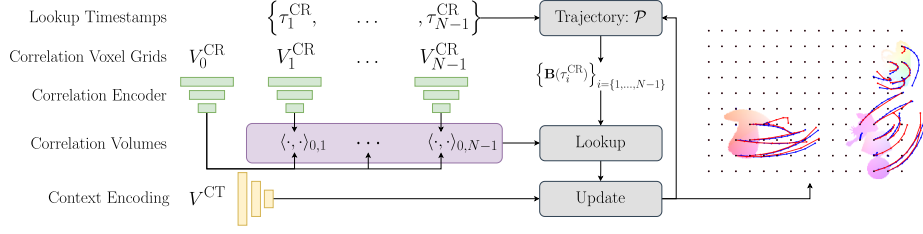


Fig. 2. Overview of the framework. For concise presentation, we illustrate the purely event-based approach. We create multiple correlation voxel grids in a sequence to compute correlation volumes. Bézier curves \mathbf{B} , parameterized by control points \mathcal{P} , represent the continuous-time pixel trajectories. Along these trajectories, we index correlation volumes at their associated timestamps. An update operator uses the output of this lookup operation to update the Bézier curves. Finally, this loop is repeated in an iterative fashion.

2.2 Continuous Tracking

Continuous-time trajectory estimation of camera poses has been proposed in the context of rolling shutter compensation [23] as well as visual-inertial odometry for event cameras [31]. Instead, we are interested in regressing pixel-trajectories, which is more closely related to high-speed feature tracking for event cameras [12,38,1,52]. Our approach is related to the work of Seok et al. [38] who use quadratic Bézier curves to sparsely track features by maximizing the variance of the image of warped events on local patches. In contrast to our work, this method can only sparsely track features where events are present, cannot incorporate learned priors from data, and does not offer the possibility to include images.

2.3 Datasets for Optical Flow

Existing datasets can be categorized as image-based optical flow datasets and event-based optical flow datasets.

Image-based The seminal work of FlowNet [8] proposed a large synthetic dataset called "FlyingChairs" to train their CNN. FlyingThings3D[29] introduced a synthetic stereo-video dataset with scene flow ground truth. AutoFlow[39] proposes to render large-scale training data with rich data augmentation in 2D for optical flow estimation. These datasets, however, do not provide event data and ground truth pixel trajectories beyond two views.

Event-based MVSEC [53] contains 5 outdoor driving sequences and 4 indoor sequences. However, optical flow ground truth from MVSEC suffers from inaccuracies in calibration [14] and only features very small displacements. DSEC-Flow, a more recent dataset, addresses these shortcomings by providing accurate but sparse optical flow groundtruth. The main downside of both MVSEC and

DSEC-Flow is that they both do not include optical flow ground truth for dynamic objects.

In contrast to the aforementioned datasets, our synthetic dataset "Multi-Flow" features accurate and dense ground truth for pixel trajectories as well as image and event data. The concept of pixel trajectories is a generalization of pixel displacement and can be used to supervise and evaluate multi-view approaches.

3 Method

The presented approach uses components from RAFT [41]. We aim at keeping this section self-contained but skip details that are explained in the aforementioned publication. Figure 2 provides an overview of the methodology.

3.1 Problem Definition

Our method is tasked with estimating a function

$$\begin{aligned} \mathbf{B} : \mathcal{T} \times \mathbb{N}_0 \times \mathbb{N}_0 &\rightarrow \mathbb{R}^2 \\ (\tau, x, y) &\mapsto \mathbf{B}(\tau, x, y) \end{aligned} \tag{1} \tag{2}$$

that describes the per-pixel trajectories in time on the image plane. $\mathcal{T} = \mathbb{R} \cap [0, 1]$ describes the domain consisting of the normalized time $\tau(t) = (t - t_r) / (t_t - t_r)$, where $\tau = 0$ corresponds to the reference time t_r from which the pixel trajectory starts and $\tau = 1$ corresponds to the target time t_t when the pixel trajectory ends. This formulation can be used to find the pixel displacement at any time between t_r and t_t .

3.2 Input Data Preparation

The proposed approach uses features extracted from event data and optionally a pair of images to further boost performance.

Multi-View Event Representations Event cameras have a fundamentally different working principle than frame-based cameras. Instead of acquiring frames, event cameras receive asynchronous events with high temporal resolution. An event $e_k(t) = (x_k, y_k, t, p_k)$ is a tuple containing information about a pixel (x_k, y_k) for which a positive or negative brightness change p_k was registered at time t . Note that the time t typically has microsecond resolution, which provides precise temporal information about motion in the scene.

The first step of the feature extraction pipeline is the construction of a discrete spatio-temporal representation from a sequence of events. For our experiments, we choose the voxel grid representation by Zhu et al. [54] due to its simplicity and possibility to extract features in a sliding window. An overview of this process is provided by Figure 3.

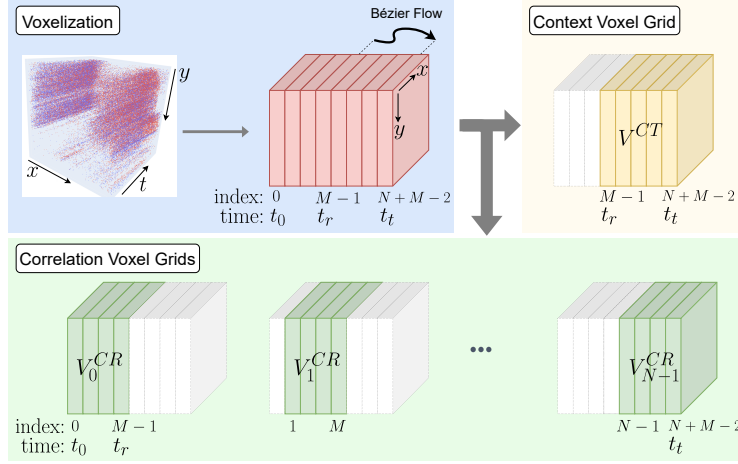


Fig. 3. Voxel Grid Generation. Events are interpolated into a voxel grid representation before being divided into sub-voxel grids that are either used as input to the context encoder or the correlation encoder.

Given the task of estimating continuous pixel trajectories from t_r , the reference time, to the target time t_t , Our method first computes a *base* voxel grid, visualized in red in Figure 3, consisting of $M + N - 1$ discrete bins along the time dimension via interpolation of event data [54]. The first M bins are computed from events prior to the reference time t_r and are required to extract the correlation features later in the pipeline. The last N bins are computed mostly from events during the time window $[t_t, t_r]$ when the pixel trajectories are estimated. These N bins are required to extract the context features. The bin at the reference timestamp t_r will be reused by both correlation and context features such that the base voxel grid consists of $M + N - 1$ bins.

From this base voxel grid, we first extract the context voxel grid V^{CT} , visualized in yellow in Figure 3. The next step is the extraction of up to N correlation voxel grids V_i^{CR} , visualized in green in Figure 3, in a sliding-window fashion from the base voxel grid. Each of these correlation voxel grids contain information about the contrast differences in the scene at slightly different times. They will later be used to guide the search for pixel trajectories via lookup operations. We refer to the correlation voxel grids also as *views* because they each represent a distinct timestamp. If we choose to extract at least two correlation voxel grids apart from the reference timestamp t_r , we label the method as *multi-view* approach. Find further algorithmic details in the appendix.

Optional Frame-based Input As we show in the experimental results, the performance of the proposed method improves if image data is used in addition to events only. To do so, we acquire a reference frame I_r at t_r and a target frame I_t at t_t . These frames contain richer information about texture at the boundary timestamps of the regressed pixel trajectories and thus simplify the correspondence search.

3.3 Feature Extraction

Features are extracted from input images and voxel grids with a convolutional network. The basic architecture of the encoders follows prior work [41,14]. The encoders extract $D = 256$ dimensional features from their input at 1/8th of the original resolution using residual blocks with striding for downsampling the feature maps. From now on, we use $H' = H/8$ and $W' = W/8$ to refer to the downsampled resolution.

The context feature encoder $f_{CT} : \mathbb{R}^{(N+3) \times H \times W} \mapsto \mathbb{R}^{D \times H' \times W'}$ concatenates the voxel grid V^{CT} with the frame I_r , if available, to extract combined features. The reference frame I_r informs the network about the absolute intensity of the reference pixels while the context voxel grid V^{CT} provides rich information about motion during the time duration of the pixel trajectories. However, contrast information is not explicitly considered yet, which will be provided by the correlation feature encoders.

The correlation encoder $f_{CR}^V : \mathbb{R}^{M \times H \times W} \mapsto \mathbb{R}^{D \times H' \times W'}$ for event representations computes features from the N correlation voxel grids in parallel, by sharing the weights. The result of this operation are N feature maps, each assigned to the timestamp associated with the last bin of each correlation voxel grid.

If in addition, a pair of frames is available, we extract image features with an additional encoder $f_{CR}^I : \mathbb{R}^{3 \times H \times W} \mapsto \mathbb{R}^{D \times H' \times W'}$.

3.4 Multi-View Correlation Volumes

We compute correlation volumes to guide correspondence search in space and time by associating subsequent views with the reference view. This association is visualized in Figure 4 and 2. We use the features created from voxel grid V_0^{CR} and optionally I_r to create the feature maps for the reference view. For each subsequent view i , we compute features from voxel grid V_i^{CR} to compute the correlation volume C_i^1 as in definition (3). This step is repeated until view $N - 1$ is reached. For the final/target view, we optionally compute a correlation volume C_I^1 from the boundary image features as in definition (4). A more detailed description is available in the supplementary material.

$$C_n^l(f_{CR}^V(V_0^{CR}), f_{CR}^V(V_n^{CR})) \in \mathbb{R}^{H' \times W' \times H'/2^l \times W'/2^l} \quad (3)$$

$$C_I^l(f_{CR}^I(I_r), f_{CR}^I(I_t)) \in \mathbb{R}^{H' \times W' \times H'/2^l \times W'/2^l} \quad (4)$$

3.5 Iterative Multi-View Flow Updates

This section describes the update scheme that uses correlation volumes introduced in the previous section 3.4.

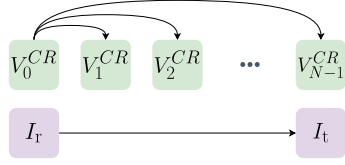


Fig. 4. Correlation-volume pairs with indicated lookup direction. The upper row shows lookups from voxel grid features and the lower row shows lookups from image features.

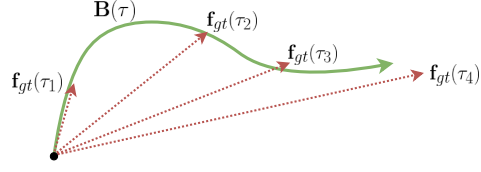


Fig. 5. Illustrative example of a Bézier prediction and $N_k = 4$ groundtruth flow maps from which the loss function (9) is computed.

Continuous-Time Flow We seek a representation of the function $\mathbf{B}(\tau, x, y)$, as introduced in equation (1), that generalizes the conventional displacement prediction of two-frame optical flow methods. To achieve this, we choose to use Bézier curves defined as

$$\mathbf{B}(\tau, x, y) = \sum_{i=0}^n \binom{n}{i} (1-\tau)^{n-i} \tau^i \mathbf{P}_i(x, y). \quad (5)$$

$\mathbf{B}(\tau, x, y)$ describes the displacement of pixel (x, y) for the normalized time $\tau \in [0, 1]$. As an example, the Bézier curves of degree $n = 1$ simply represent a linear trajectories in space and time that is fully described by \mathbf{P}_1 . The task of our method, however, is to regress the parameter set

$$\mathcal{P} = \{\mathbf{P}_1, \dots, \mathbf{P}_n\} \quad (6)$$

$\mathbf{P}_0 = \mathbf{0}$ does not have to be estimated because it defines the starting point of the trajectory that coincides with the reference pixels. The advantages of working with Bézier curves is that they are fast to evaluate and can be concisely summarized by a set of parameters \mathcal{P} .

The degree of the Bézier curves is a fixed parameter. We found that it is best to set it equal to the number of supervision points along the trajectory for an accurate trajectory prediction (details in supplementary material).

Iterative Bézier Updates The Bézier curves are initialized with $\mathbf{B} = \mathbf{0}$ such that $\mathcal{P} = \{\mathbf{0}, \dots, \mathbf{0}\}$. Each iteration adds an update to the parameter set \mathcal{P} : $\mathbf{P}_i^{k+1} = \mathbf{P}_i^k + \Delta \mathbf{P}_i$, $\forall i \in \{1, \dots, n\}$

Multi-View Correlation Lookup Similar to the original RAFT implementation, we use lookup operations to extract features from the correlation volumes. In contrast, however, we extract features from multiple correlation volumes, each associated to a unique normalized timestamp. Given the current estimate of the Bézier control points \mathcal{P} , we map each pixel $\mathbf{x} = (x, y)$ at time $\tau = 0$ to the estimated corresponding pixel location $\mathbf{x}'(\tau) = (x'(\tau), y'(\tau))$ at time τ :

$$\mathbf{x}'(\tau) = \mathbf{x} + \mathbf{B}(\tau, \mathbf{x}) \quad (7)$$

Similar to RAFT, the lookup is performed in a local neighborhood \mathcal{N} around the corresponding pixel location $\mathbf{x}'(\tau)$:

$$\mathcal{N}(\mathbf{x}'(\tau)) = \{\mathbf{x}'(\tau) + \mathbf{dx} \mid \mathbf{dx} \in \mathbb{Z}^2, \|\mathbf{dx}\|_\infty \leq r\} \quad (8)$$

Lookups are performed on all available correlation volumes with bilinear sampling. We use a constant lookup radius of $r = 4$, as in the original RAFT implementation, to increase the effective lookup radius. Finally, the values from the union of lookup operations is concatenated into a single feature map.

Upsampling of Bézier Curves The Bézier control points are estimated at $1/8$ -th of the original resolution. Since $\mathbf{B}(\cdot)$ is linear in the control points \mathcal{P} , we can upsample the Bézier curves to the full resolution using convex upsampling [41]. As a result, the Bézier curves at the full resolution will be a learned convex combination of 3×3 grids of Bézier curves at the lower resolution.

3.6 Supervision

We supervise the model with N_k ground truth flow maps along the trajectory, visualized in Figure 5.

$$\mathcal{L} = \frac{1}{N_k} \sum_{i=1}^{N_i} \gamma^{N_i-i} \sum_{k=1}^{N_k} \|\mathbf{f}_{gt}(\tau_k) - \mathbf{B}_i(\tau_k)\|_1 \quad (9)$$

where \mathbf{B}_i is the Bézier curve at iteration i , $\tau_k \in [0, 1]$ are the evaluation timestamps of the Bézier curves, and $\gamma = 0.8$. For a single displacement map, such as in two-frame optical flow, the corresponding parameters are $N_k = 1$ and $\tau_1 = 1$.

4 MultiFlow Dataset

To the best of our knowledge, there are no publicly available datasets with ground truth for pixel trajectories, which is more general than pixel displacements, in combination with events and images. Therefore, we create a new synthetic dataset to evaluate the proposed approach.

4.1 Data Generation Procedure

We generate 9895 training and 1985 test sequences in simulation for MultiFlow. The background images are sampled from the Flickr30K dataset [48]. The foreground objects are extracted from 650 PNG images, 450 for training and 200 for testing, by masking out transparent regions using the alpha channels.

The duration of each sequence is defined to be one second. We randomly sample 3 to 4 data points over similarity transformations in 2D for each foreground and background object. Interpolation with piecewise cubic spline polynomials

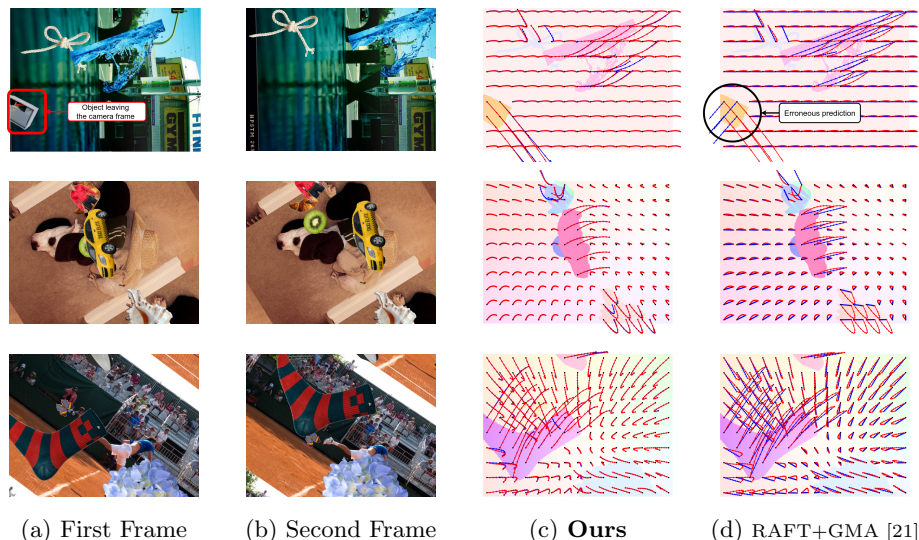


Fig. 6. Predictions of our method (c) and the strongest baseline, RAFT+GMA [21] (d), on the MultiFlow dataset. Predictions are shown in blue and the ground truth trajectory is visualized in red. The background is a colorization of the ground truth flow to highlight moving objects. Events are not shown for conciseness but are also used by our method. Best viewed in PDF form.

provide the continuous-time transformation of all objects throughout the duration of each sequence. The generated similarity transformation trajectories are used to both render images and compute ground truth pixel trajectories. To generate events, we use ESIM [35] on frames rendered at 1000 frames per second on the full sequence. We refer to the supplementary material for dataset examples and a more detailed description.

5 Experiments

This section has four distinct purposes. First, to show quantitative real-world performance on DSEC-Flow on traditional two-view metrics. Second, to show quantitative performance on the *main task* on MultiFlow: predicting continuous-time pixel trajectories. Third, to show qualitative performance for sim2real transfer using models trained on our MultiFlow dataset. Finally, an ablation study highlights the importance of the proposed components.

Implementation Details Our models are implemented in Pytorch and trained from scratch with random weights on each dataset. We use AdamW [26] with gradient clipping in the range of $[-1, 1]$ and a OneCycle learning rate with 200k iterations and a batch size of 3. On both datasets, we perform random horizontal and vertical flipping as well as random cropping of the input data. For all experiments, our method uses 5 views to compute the cost volumes.

	Input	EPE	AE	1PE	2PE	3PE
EV-FlowNet [53]	E	2.32	-	55.4	29.8	18.6
E-RAFT [14]	E	0.79	2.85	12.74	4.74	2.68
RAFT [41]	I	0.78	<u>2.44</u>	12.40	4.60	2.61
RAFT + GMA [21]	I	0.94	2.66	12.98	5.08	2.96
Ours	E	<u>0.75</u>	2.68	<u>11.90</u>	<u>4.41</u>	<u>2.44</u>
Ours	E+I	0.69	2.42	9.70	3.42	1.88

Table 1. Results on DSEC-Flow. Our method outperforms prior work even when only using events. Adding image data further improves performance.

5.1 DSEC-Flow

DSEC-Flow [14,13] is a driving dataset with stereo event and global shutter cameras. The purpose of this experiment is to show the quantitative performance of our approach on real-world data. However, we can only test on traditional two-view optical flow metrics because no pixel trajectory ground truth is available on DSEC-Flow. In other words, for displacement prediction, the quality of the intermediate continuous trajectory is irrelevant. Instead, only the final displacement prediction is evaluated using end-point-error (EPE) and angular error (AE) metrics [3]. We also report the X -point error, a metric that reports the percentage of pixels with EPE higher than X pixels.

For our experiments that combine image and event data, we warp images to the event camera. Due to the small baseline between both cameras, we can warp the image to a plane at an infinite depth and re-project it into the event camera coordinate frame. The disparity is negligible.

We use $M = N = 5$ bins for both the context and correlation voxel grid (see Section 3.2). We also experimented with a higher number of bins but did not observe significant improvements. Our model is supervised with the 2-view version of our loss proposed in equation (9). This loss function is used because DSEC-Flow only provides ground truth for pixel displacements. Finally, we choose a degree of 2 for the Bézier curves mostly to account for non-linear motion due to change in depth.

The performance of EV-FlowNet [53] and E-RAFT is taken from Gehrig et al. [14]. We additionally train the frame-based RAFT model [41] and GMA [21], an addition over RAFT, to also compare against purely frame-based approaches.

Quantitative Evaluation Table 1 summarizes our results on the DSEC-Flow test set. Our approach, using both event data and frames, achieves 0.69 EPE which is 11.5% lower than RAFT [41] and 8 % lower than our own method using only event data. Furthermore, our purely event-based approach achieves an EPE of 0.75 which is 5% lower than the EPE of 0.79 that E-RAFT achieves. Overall the performance of E-RAFT [14] is comparable to RAFT while EV-FlowNet [53] is not competitive. In our experiments, the GMA version of RAFT does not outperform the RAFT baseline on this dataset.

	Input	Trajectory Metrics		2-View Metrics	
		TEPE	TAE	EPE	AE
E-RAFT [14]	E	(6.70)	(18.44)	7.56	6.19
RAFT [41]	I	(6.89)	(19.31)	7.42	6.71
RAFT + GMA [21]	I	(5.14)	(16.35)	1.22	1.30
Ours	E	<u>1.48</u>	<u>3.64</u>	2.69	3.86
Ours	E+I	1.08	2.77	<u>1.88</u>	<u>2.70</u>

Table 2. Results on MultiFlow. TEPE and TAE are the trajectory version of EPE and AE. Metrics in brackets are computed using a linear motion model because these method are not able to estimate trajectories.

These results indicate that the proposed method, even though designed to work for regressing pixel trajectories, is competitive with two-view approaches on the task of pixel displacement prediction. Note that we have not used any additional ground truth information compared to the baselines.

5.2 MultiFlow

The experiments on MultiFlow assess the pixel trajectory regression capabilities. To achieve this, we introduce an extension of EPE and AE to trajectories.

$$\text{TEPE} = \frac{1}{N_k} \sum_k^{N_k} \text{EPE}(\mathbf{f}_{pred}(t_k), \mathbf{f}_{gt}(t_k)) \quad (10)$$

We define TAE in an analogous way.

We train three previously published baselines for an extensive comparison. First, RAFT [41] and RAFT+GMA [21] for a comparison against frame-based approaches. Second, E-RAFT [14] for a comparison against a recent event-based approach. We focus on these architectures because they are related to our approach and achieve state-of-the-art performance on public benchmarks [7,13]. We train our method on the loss defined by equation (9) while the two-view approaches are trained on the two-view version of the loss [41]. We supervise our methods with 10 flow maps along the trajectory using loss (9) and set the Bézier curve degree to 10 according to section 3.5.

Quantitative Evaluation Table 2 summarizes the quantitative results. The baseline models are only able to predict pixel displacements. Therefore, for a fairer comparison, we use a linear motion model to compare against our methods on the trajectory metrics TEPE and TAE. Our methods achieve up to 4.8 times lower trajectory end-point errors compared to linear motion model baselines. This discrepancy occurs mostly because our models are successfully predicting the pixel trajectories while the linear motion model is insufficient for the complexity of pixel motion in this dataset. As expected, combining events and frames further improves performance by a large margin on all metrics for our approaches. Both RAFT [41] and E-RAFT [14] underperform compared to our

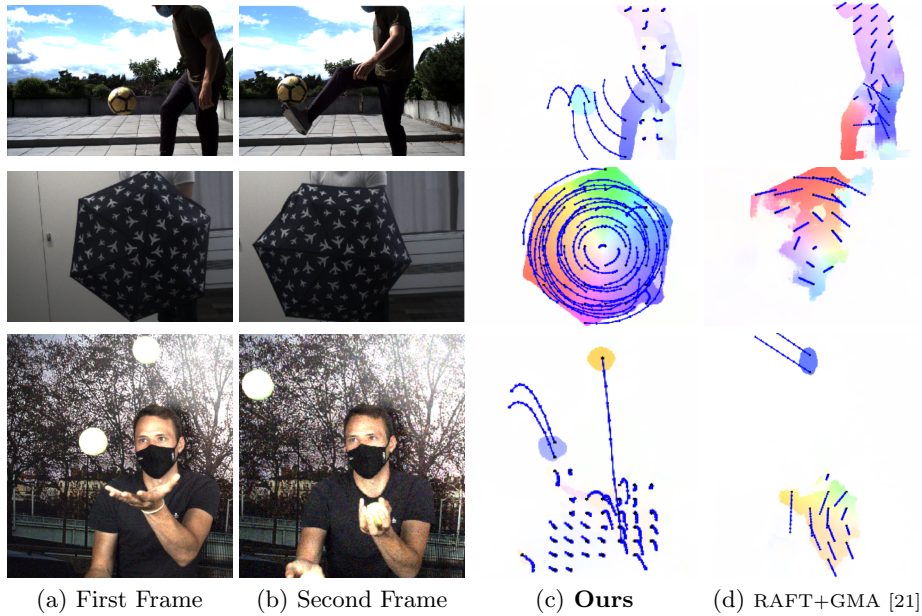


Fig. 7. Predictions of our method (c) and RAFT+GMA [21] (d), on the HS-ERGB [42] dataset. Predictions are shown in blue. The background is a colorization flow to highlight moving objects. Events are not shown for conciseness.

approach on the 2-view metrics for which they were designed. A notable exception is the RAFT+GMA [21] which performs best on the 2-view metrics among all methods. However, RAFT+GMA is not designed for trajectory prediction and therefore falls short in TEPE and TAE compared to our approach.

Qualitative Analysis Figure 6 illustrates the predictions of our model, using events and frames, in comparison to RAFT+GMA [21]. Our approaches successfully predict the continuous trajectory, even if the objects leave the field of view. This is not the case for the two-view method RAFT+GMA, as seen in the first row of Figure 6. Evidently, it fails at predicting the motion of objects that are missing in the second view because it is impossible to establish a match. The second row shows that our method can accurately predict pixel trajectories while RAFT+GMA does well in predicting the final pixel displacement.

5.3 Qualitative Sim2Real Results

To qualitatively assess the real-world capabilities of our method, we use our purely event-based model, trained only on the simulation dataset MultiFlow, and show predictions on the HS-ERGB dataset [42] in Figure 7. Although our method is only trained on MultiFlow, it can correctly predict non-linear motion of moving objects while the frame-based baseline [21] fails due to large motion and ambiguities in the input frames.

	Input	Trajectory Metrics		2-View Metrics	
		TEPE	TAE	EPE	AE
w/o Bézier	E+I	6.26	18.16	6.46	5.23
w/o multi-view	E+I	1.56	3.73	2.29	3.13
<u>Reference</u>	E+I	<u>1.08</u>	<u>2.77</u>	<u>1.88</u>	<u>2.70</u>
w/o Bézier	E	6.55	18.39	6.98	5.87
w/o multi-view	E	2.24	5.14	3.76	5.03
<u>Reference</u>	E	<u>1.48</u>	<u>3.64</u>	<u>2.69</u>	<u>3.86</u>

Table 3. Ablation experiments on MultiFlow. Final model settings are underlined.

5.4 Ablation Study

We study the contributions of the two main components of our approach on the MultiFlow dataset, summarized in Table 3. The two reference models are the full models as described in the methodology. First, we remove the Bézier curve regression and note a drastic drop in performance on all metrics. Removing the Bézier curves is equivalent to assuming linear motion. Linear motion is not representative for this dataset and hampers the correlation lookup. Second, we remove the multi-view lookup scheme and note that both TEPE and EPE increase between 22% and 51% with respect to the event-based and hybrid reference model. We conclude that both components are important for achieving the best results. Ablation studies on the loss function (9) and Bézier curve degree as well as runtime and parameter details can be found in the appendix.

6 Conclusion

We have introduced a method for estimating continuous-time pixel trajectories from events and frames. The proposed approach regresses Bézier curves and uses the pixel trajectories to extract correlation features. Our experimental results demonstrate that the proposed method can accurately predict continuous pixel trajectories while at the same time outperforming strong baselines not only in simulation but also on real data. Finally, our sim2real results suggest that the new MultiFlow dataset can also be used to pretrain pixel trajectory regression models for downstream applications.

7 Acknowledgment

This work was supported by Huawei Zurich Research Center; by the National Centre of Competence in Research (NCCR) Robotics (grant agreement No. 51NF40-185543) through the Swiss National Science Foundation (SNSF), and the European Research Council (ERC) under grant agreement No. 864042 (AG-ILEFLIGHT).

Appendix

8 Additional Ablation Studies and Model Details

This section provides additional ablation studies and runtime metrics for the interested reader.

8.1 Degree of the Bézier Curves

The goal of this experiment is to answer the question: **Which Bézier curve degree is appropriate for my model?**

To answer this question, we train 4 different models with Bézier curve degrees 1, 5, 10 and 15 using frames and events as input to the model. The supervision on pixel trajectories at training time is at 20 Hz, that we supervise the model on the pixel trajectory every 50 milliseconds.

Bézier Degree	TEPE		TAE	
	20 Hz	100 Hz	20 Hz	100 Hz
1	6.26	6.00	18.16	18.68
5	1.18	1.10	3.06	3.09
10	1.08	1.01	2.77	2.99
15	1.04	1.02	2.70	3.46

Table 4. Trajectory errors of our method with a varying number of Bézier curve degree evaluated with either 20 Hz (every 50 ms) or 100 Hz (every 10ms) ground truth along the trajectories. All variants were trained with trajectory supervision at 20 Hz. Although a Bézier degree of 15 improves the 20 Hz performance, the error metrics increase when the evaluation takes place at 100 Hz. Best performance in bold.

Intuitively, one would think that a higher Bézier degree always improves the performance. Table 4 indeed shows that a higher Bézier degree improves performance, when the models are evaluated at 20 Hz. The models were also trained with a supervision signal at 20 Hz, that is with supervision at regular time intervals of 50 milliseconds. Interestingly, an evaluation of these models at a higher frequency of 100 Hz reveals a decrease in performance for the model with a Bézier degree of 15. The reason for that is that we observe a test-time overfitting of the predicted trajectory at the timestamps on which the model was supervised. In our case, we supervised the model at regular intervals of 50 milliseconds. An evaluation on the same timestamps does not reveal this phenomenon, which is why an evaluation at 100 Hz is required.

Hence, the answer to the original question is: **For accurate pixel trajectory predictions, the Bézier degree should be chosen equal to the number of supervision points along the pixel trajectories.**

The degree can be set higher than the number of supervision points to improve performance on the timestamps of interest. However, the pixel trajectories may not be as accurate anymore. An example for this is our DSEC-Flow experiments where we have only 1 supervision point (2-view) but found that a Bézier degree of 2 improves the performance on the 2-view metric. This is a reasonable approach as long as the downstream application does not require accurate pixel trajectories.

8.2 Loss Function

This experiment examines the influence of the trajectory loss on trajectory and 2-view metrics. We train 2 additional models with the 2-view loss. One using only events and a second one using both frames and events. Table 5 summarizes the results.

For both input variations, the error metrics substantially decrease when the model is trained with the trajectory loss. This reduction is evident for both the trajectory metrics and also the 2-view metrics. This indicates, that the trajectory loss function is a better choice for the proposed method than the 2-view loss.

Finally, the results in Table 5 indicate that we could further reduce the errors of the DSEC-Flow experiment with the appropriate ground truth.

	Input	Trajectory Metrics		2-View Metrics	
		TEPE	TAE	EPE	AE
2-View Loss	E+I	16.18	19.37	2.96	4.19
Trajectory Loss	E+I	<u>1.08</u>	<u>2.77</u>	<u>1.88</u>	<u>2.70</u>
2-View Loss	E	16.73	21.63	5.80	8.71
Trajectory Loss	E	<u>1.48</u>	<u>3.64</u>	<u>2.69</u>	<u>3.86</u>

Table 5. The trajectory loss refers to the loss function of equation (10) of the main paper, with $N_k > 1$. The 2-View loss refers to the same loss function with $N_k = 1$. Training our method with the trajectory loss leads to drastically lower errors even for the 2-View metrics.

8.3 Number of Correlation Lookups

Table 6 shows that increasing the number of correlation lookups improves performance consistently on all metrics. However, substantially increasing the number of correlation volumes incurs higher memory consumption and increases computational demand. This result suggests a trade-off between performance and compute and memory requirements.

Note that the number of correlation volumes is the number of correlation lookups (in time) + 1 because the correlation volume at the reference time has to be accounted for.

# Correlation Lookups	Trajectory Metrics		2-View Metrics	
	TEPE	TAE	EPE	AE
1	1.56	3.73	2.29	3.13
3	1.13	2.87	1.96	2.75
<u>5</u>	<u>1.08</u>	<u>2.77</u>	<u>1.88</u>	<u>2.70</u>

Table 6. Increasing the number of correlation volumes/lookups in time improves performance. The underlined row refers to the reference model used in the experiments.

8.4 Runtime Metrics

Table 7 shows inference time in milliseconds, parameter count in millions of parameters and memory consumption at inference time in Gigabytes on samples from the MultiFlow dataset. Overall, our proposed method has higher demands on the presented metrics compared to RAFT [41], which is expected because it is a generalization of the RAFT architecture.

	Input	Inference time [ms]	Params	Memory [GB]
RAFT [41]	I	61	5.3 M	1.20
Ours	E	76	5.6 M	1.65
Ours	E+I	97	5.9 M	1.65

Table 7. Comparison of inference time, parameter count and memory consumption on MultiFlow. These numbers have been obtained on a Titan RTX GPU with an implementation using Pytorch version 1.10.2

9 Implementation Details

This section supplements the main paper with more detailed descriptions of selected parts of the methodology.

9.1 Input Data Preparation

Multi-View Event Representations Event cameras have a fundamentally different working principle than frame-based cameras. Instead of acquiring frames, event cameras receive asynchronous events with high temporal resolution. An event $e_i = (x_i, y_i, t_i, p_i)$ is a tuple containing information about a pixel (x_i, y_i) for which a positive or negative brightness change p_i was registered at time t_i . Time t_i typically has microsecond resolution, which provides precise temporal information about motion in the scene.

The first step of the feature extraction pipeline is the construction of a discrete spatio-temporal representation from a sequence of events. For our experiments, we choose the voxel grid representation by Zhu et al. [54] due to its simplicity and possibility to extract features in a sliding window. An overview of this process is provided by Figure 3.

Given the task of estimating continuous pixel trajectories from t_r , the reference time, to the target time t_t , we first compute the temporal discretization $\Delta t = \frac{t_t - t_r}{N-1}$. N is the number of bins that we later use to compute context features from event data. Having computed Δt , we choose M to be the number of bins that we will use to compute correlation features from event data. The bin with index $M - 1$ corresponds to the reference timestamp t_r and will be reused by both correlation and context features such that the *base* voxel grid consists of $M + N - 1$ bins. This base voxel grid is visualized in red in Figure 3, and we compute it as follows:

$$\begin{aligned} t_i^* &= (M + N - 1)(t_i - t_0)/(t_t - t_0) \\ V(x, y, t) &= \sum_{e_i | t_i \in [t_0, t_t]} p_i k_b(x - x_i) k_b(y - y_i) k_b(t - t_i^*) \\ k_b(a) &= \max(0, 1 - |a|) \end{aligned} \quad (11)$$

where $t_0 = t_r - \Delta t \cdot (M - 1)$ and k_b is the bilinear interpolation kernel [17].

Figure 3 shows how we extract sub-voxel-grids from the overall voxel grid with $M + N - 1$ bins. To provide contextual information to the network, we extract a context voxel grid $V^{CT} \in \mathbb{R}^{N \times H \times W}$ which is visualized in yellow in Figure 3. It consists of N bins starting with the bin at index $M - 1$, associated with t_r , to the target time t_t associated with the final bin at index $N + M - 2$. For the correlation encoder, we extract a maximum of N voxel grids $V_i^{CR} \in \mathbb{R}^{M \times H \times W}$, $i \in 0, 1, \dots, N - 1$, visualized in green in Figure 3, consisting of M bins each in a sliding window fashion.

Note that N is the maximum number of correlation voxel grids but typically only a subset is used for a better trade-off between compute and performance.

9.2 Multi-View Correlation Volumes

We compute correlation volumes to guide correspondence search in space and time by associating subsequent views with the reference view. This association is visualized in Figure 4. We use the features computed from voxel grid V_0^{CR} and optionally I_r to create the feature maps for the reference view. For each subsequent view i , we compute features from voxel grid V_i^{CR} to compute the correlation volume C_i^1 as in definition (12). This step is repeated until view $N - 1$ is reached. For the final/target view, we optionally compute a correlation volume C_I^1 from the boundary image features as in definition (13).

$$\mathbf{C}_n^l(f_{\text{CR}}^V(V_0^{\text{CR}}), f_{\text{CR}}^V(V_n^{\text{CR}})) \in \mathbb{R}^{H' \times W' \times H'/2^l \times W'/2^l} \quad (12)$$

$$\mathbf{C}_I^l(f_{\text{CR}}^I(I_r), f_{\text{CR}}^I(I_t)) \in \mathbb{R}^{H' \times W' \times H'/2^l \times W'/2^l} \quad (13)$$

$$C_{ijkl}(a, b) = \sum_h a_{ijh} \cdot b_{klh} \quad (14)$$

Overall, this process results in a set of correlation volumes expressed in definitions (15), (16) and (17).

$$\mathcal{C}_V = \left\{ \{\mathbf{C}_1^1, \dots, \mathbf{C}_1^{L_1}\}, \dots, \{\mathbf{C}_{N-1}^1, \dots, \mathbf{C}_{N-1}^{L_{N-1}}\} \right\} \quad (15)$$

$$\mathcal{C}_I = \left\{ \mathbf{C}_I^1, \dots, \mathbf{C}_I^{L_I} \right\} \quad (16)$$

$$\mathcal{C} = \mathcal{C}_V \cup \mathcal{C}_I \quad (17)$$

The set of final correlation volumes also incorporates $L_i - 1$ pooled, lower resolution correlation volumes. We found that it is sufficient to use the following setting in our experiments:

- $L_I = 4$ and $L_{N-1} = 4$: Correlation lookup for the final target view requires a large receptive field, otherwise the trajectories might not converge to the end-point.
- $L_i = 1$, $i = \{1, \dots, N-2\}$: These intermediate correlation volumes are mostly used to guide the pixel trajectories locally to accurate correspondences.

10 MultiFlow Dataset Generation

This section provides a more formal and detailed overview of the data generation process that was used to create the MultiFlow dataset.

The duration of each sequence in the dataset is fixed to one second. We sample either 3 or 4 (random choice of 50% probability each) control points in the space of pixel translation, scale, and rotation of the foreground (FG) and background (BG) objects in the image plane. The time assigned to control points is sampled from the range $[0, 1]$ while ensuring strictly increasing values to maintain the temporal order.

The control points are sampled according to the following discrete-time process with parameters shown in Table 8:

$$X_{k+1} = \begin{cases} \hat{\gamma} \cdot \hat{X}_{k+1}^{\text{Det}} + (\hat{\gamma} - 1) \cdot \hat{X}_{k+1}^{\text{Stoch}} & (\hat{\alpha} = 0) \wedge (\hat{\beta} = 0) \\ X_k & (\hat{\alpha} = 1) \vee (\hat{\beta} = 1) \end{cases} \quad (18)$$

where

$$\hat{X}_{k+1}^{\text{Det}} = X_k + \frac{t_{k+1} - t_k}{t_k - t_{k-1}} (X_k - X_{k-1}) \quad (19)$$

refers to the deterministic part of the process that uses a constant velocity model. It is inspired by the law of conservation of momentum from classical mechanics. t_k is the time associated with control point k . To introduce more variability in the data generation process, we introduce a stochastic process:

$$\text{Translation \& Rotation: } \hat{X}_{k+1}^{\text{Stoch}} = X_k + \Delta X \quad \Delta X \sim \text{Uni}(-\theta, \theta) \quad (20)$$

$$\text{Scale: } \hat{X}_{k+1}^{\text{Stoch}} = X_k \cdot \Delta X \quad \Delta X \sim (1 + \delta_0)^{(2\delta_1-1)}, \quad (21)$$

$$\delta_0 \sim \text{Uni}(0, \theta), \quad \delta_1 \sim \text{Bern}(0.5)$$

Uni stands for the continuous uniform distribution and *Bern* refers to the Bernoulli distribution.

$\hat{\alpha} \sim \text{Bern}(\alpha)$ models the probability that the similarity transformation (translation, rotation *and* scale) of the object remains constant during the whole sequence.

$\hat{\beta} \sim \text{Bern}(\beta)$ is sampled separately for each component (translation, rotation *or* scale) of the similarity transformation and models the probability that the component remains constant during the sequence.

$\hat{\gamma} \sim \text{Uni}(0, \gamma)$ is sampled separately for each component (translation, rotation *or* scale) of the similarity transformation and models the degree of the constant velocity component. For $\hat{\gamma} = 1$, the new control point is computed deterministically with a constant velocity model according to equation (19). $\hat{\gamma} = 0$ corresponds to a purely stochastic update according to equations (20) or (21). $\hat{\gamma} \in (0, 1)$ results in a convex combination of both as shown in equation (18).

Component	α	β	γ	θ
Translation BG	0.1	0	0.8	30
Rotation BG		0.7	0.6	10
Scale BG		0.4	0.3	0.15
Translation FG	0	0	0.9	120
Rotation FG		0.3	0.6	30
Scale FG		0.3	0.3	0.30

Table 8. Parameters of the distribution of the transformation coefficients for foreground objects (FG) and background (BG). The values of θ are shown in *pixels* for translation, in *degree* for rotation and in *dimensionless quantity* for scale. The values of α affect the overall similarity transformation and therefore belong to translation, rotation and scale simultaneously.

We compute continuous-time trajectories over similarity transformations via cubic spline interpolation on the $K \in \{3, 4\}$ acquired control points X_0, \dots, X_{K-1} . It would be possible to sample a higher number of control points, but we found

that 4 control points are sufficient to capture interesting non-linear motion that we could also observe in real-world applications of our algorithm (see Figure 7 of the main paper).

Pixel Trajectory Ground Truth The ground truth for the pixel trajectories is computed with respect to a reference time at 0.4 seconds. The pixel trajectory is expressed as pixel displacements at different target timestamps with respect to the original pixel location at the reference time. Overall, the dataset consists of pixel trajectory ground truth at intervals of 10 milliseconds up to time 0.9 seconds. The first 0.4 and last 0.1 seconds can be used as additional context. In our experiments, we use events until timestamp 0.4 seconds to build the first correlation voxel grid (index 0 to $M - 1$ in Figure 3). Less context leads to less expressive correlation features which lead to a trade-off between dataset size and context information.

11 Experimental Details on MultiFlow

We generate a voxel grid with 65 bins using events from $t = 0.1$ to $t = 0.9$. Our experiments with substantially lower number of bins (e.g. 9 as in the DSEC-Flow experiments) led to suboptimal performance. We observed that the reason for this is the overwriting of polarities in the voxel grid. Increasing the temporal resolution of the voxel grid alleviates this problem. The 65 bins of the voxel grid are then divided into a context voxel grid with $N = 41$ bins and 6 correlation voxel grids with $M = 25$ bins each (see Figure 3). The correlation voxel grids are extracted in regular intervals of 8 such that the 25th bin corresponds to the reference time and the 65th bin corresponds to the final timestamp of the trajectory. With these 6 correlation voxel grids we can compute 5 lookup tables in time to guide the pixel trajectory search of the network. In principle, we could also have up to 25 correlation voxel grids with this setup, but that would incur an unreasonable amount of memory and computational overhead with minimal gain in performance, as indicated in Table 6.

Qualitative predictions of our model, using events and frames, on the test set of MultiFlow are shown in Figure 8.

12 Geometric Motivation: Non-linear Continuous Flow is Omnipresent

Continuous-time motion of pixels in image space are in general non-linear in either space and/or time. To illustrate this, consider a simple scenario of a camera moving along the principle axis with velocity v in a static scene with a single 3D point P with depth D at $t = 0$. In the camera frame, P is moving towards the camera plane:

$$P(t) = (X, Y, Z(t)), \quad Z(t) = D - v \cdot t \quad (22)$$

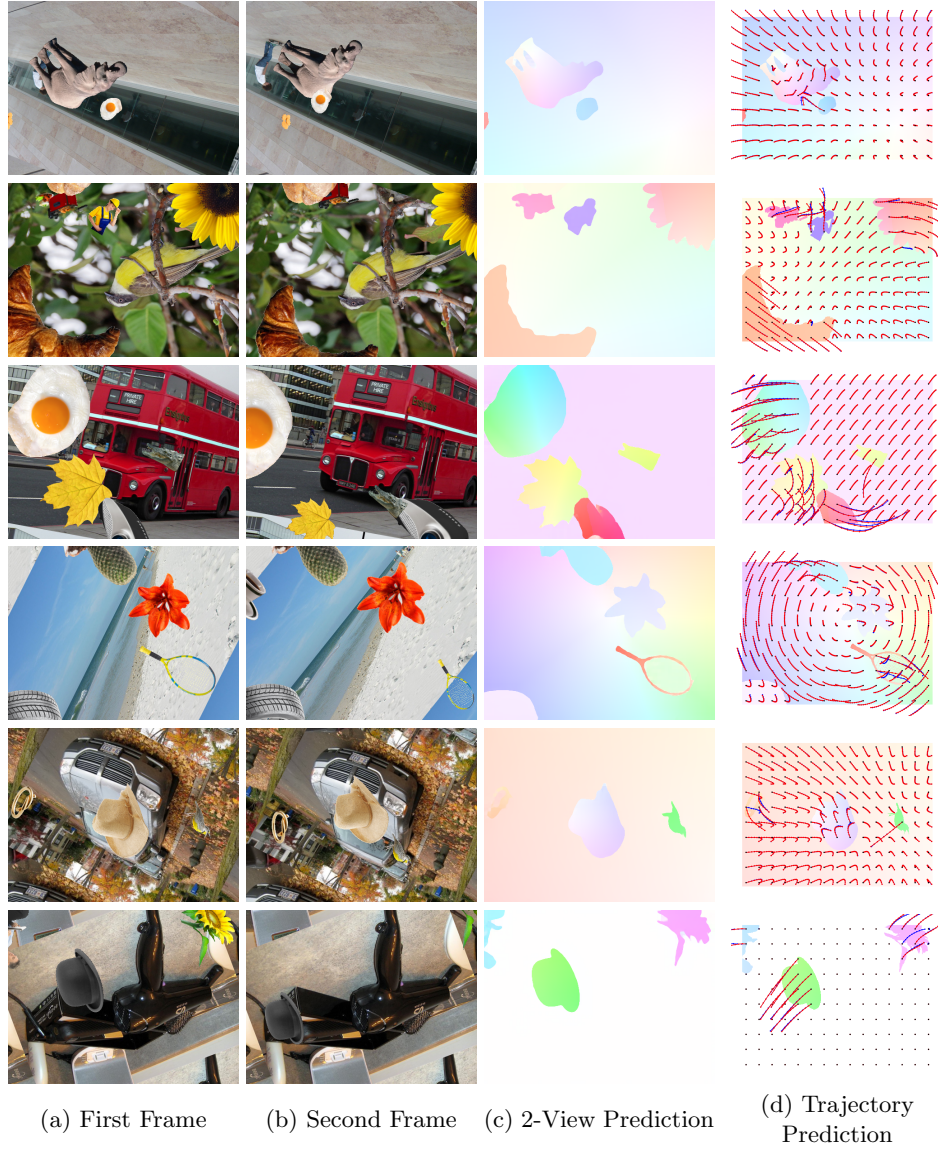


Fig. 8. Predictions of our model (E+I) on our MultiFlow test set. (a) shows the frame at the reference time, (b) the frame at the final timestamp of the trajectory, (c) shows the predicted pixel displacement between reference and final timestamp, and (d) shows the full prediction of the pixel trajectories. The predicted trajectory is shown in blue and the ground truth in red. The background of (d) is the colorization of the 2-view ground truth.

Assuming a focal length f and principle point (x_0, y_0) , the point trajectory $p(t) = (x(t), y(t))$ on the image plane is

$$p(t) = \begin{bmatrix} f \cdot \frac{X}{D - v \cdot t} + x_0 \\ f \cdot \frac{Y}{D - v \cdot t} + y_0 \end{bmatrix} \quad (23)$$

Hence, the projected trajectory $p(t)$ appears linear in the image plane (x, y) but non-linear in time t . Therefore, even in this simple scenario, we require a trajectory that departs from the linearity assumption.

Indeed, scenes with purely linear (in space and time) pixel trajectories are rare special cases. For example, a static camera observing a rigid dynamic object undergoing pure translation with constant velocity parallel to the principle plane of the camera in an otherwise static scene.

This motivates us to model pixel motion with Bézier curves that can adapt to non-linear motion in space and time. In principle, it is also possible to regress discrete trajectories and fit a spline through them. However, this approach would complicate the implementation significantly, especially if we require control points in non-uniform time intervals.

References

1. Alzugaray López, I., Chli, M.: Haste: Multi-hypothesis asynchronous speeded-up tracking of events. In: British Mach. Vis. Conf. (BMVC) (2020)
2. Bailer, C., Varanasi, K., Stricker, D.: Cnn-based patch matching for optical flow with thresholded hinge embedding loss. In: IEEE Conf. Comput. Vis. Pattern Recog. (CVPR) (July 2017)
3. Baker, S., Lewis, D.S.J., Roth, S., Black, M.J., Szeliski, R.: A database and evaluation methodology for optical flow. *Int. J. Comput. Vis.* **92**(1), 1–31 (2011)
4. Bardow, P., Davison, A.J., Leutenegger, S.: Simultaneous optical flow and intensity estimation from an event camera. In: IEEE Conf. Comput. Vis. Pattern Recog. (CVPR). pp. 884–892 (2016). <https://doi.org/10.1109/CVPR.2016.102>
5. Benosman, R., Ieng, S.H., Clercq, C., Bartolozzi, C., Srinivasan, M.: Asynchronous frameless event-based optical flow. *Neural Netw.* **27**, 32–37 (2012). <https://doi.org/10.1016/j.neunet.2011.11.001>
6. Butler, D.J., Wulff, J., Stanley, G.B., Black, M.J.: A naturalistic open source movie for optical flow evaluation. In: Eur. Conf. Comput. Vis. (ECCV) (Oct 2012)
7. Butler, D.J., Wulff, J., Stanley, G.B., Black, M.J.: A naturalistic open source movie for optical flow evaluation. In: Eur. Conf. Comput. Vis. (ECCV) (2012)
8. Dosovitskiy, A., Fischer, P., Ilg, E., Häusser, P., Hazırbaş, C., Golkov, V., van der Smagt, P., Cremers, D., Brox, T.: FlowNet: Learning optical flow with convolutional networks. In: Int. Conf. Comput. Vis. (ICCV). pp. 2758–2766 (2015). <https://doi.org/10.1109/ICCV.2015.316>
9. Gadot, D., Wolf, L.: Patchbatch: A batch augmented loss for optical flow. In: IEEE Conf. Comput. Vis. Pattern Recog. (CVPR) (June 2016)
10. Gallego, G., Delbruck, T., Orchard, G., Bartolozzi, C., Taba, B., Censi, A., Leutenegger, S., Davison, A., Conradt, J., Daniilidis, K., Scaramuzza, D.: Event-based vision: A survey. *IEEE Trans. Pattern Anal. Mach. Intell.* (2020). <https://doi.org/10.1109/TPAMI.2020.3008413>
11. Garg, R., Roussos, A., Agapito, L.: A variational approach to video registration with subspace constraints. *Int. J. Comput. Vis.* **104**(3), 286–314 (2013)
12. Gehrig, D., Rebecq, H., Gallego, G., Scaramuzza, D.: EKLt: Asynchronous photometric feature tracking using events and frames. *Int. J. Comput. Vis.* (2019). <https://doi.org/10.1007/s11263-019-01209-w>
13. Gehrig, M., Aarents, W., Gehrig, D., Scaramuzza, D.: Dsec: A stereo event camera dataset for driving scenarios. *IEEE Robot. Autom. Lett.* (2021)
14. Gehrig, M., Millhäusler, M., Gehrig, D., Scaramuzza, D.: E-RAFT: Dense optical flow from event cameras. In: 3D Vision (3DV) (2021)
15. Godet, P., Boulch, A., Plyer, A., Besnerais, G.L.: Starflow: A spatiotemporal recurrent cell for lightweight multi-frame optical flow estimation. In: IEEE Int. Conf. Pattern Recog. (ICPR). pp. 2462–2469 (2021). <https://doi.org/10.1109/ICPR48806.2021.9412269>
16. Ilg, E., Mayer, N., Saikia, T., Keuper, M., Dosovitskiy, A., Brox, T.: FlowNet 2.0: Evolution of optical flow estimation with deep networks. In: IEEE Conf. Comput. Vis. Pattern Recog. (CVPR). pp. 1647–1655 (2017). <https://doi.org/10.1109/cvpr.2017.179>
17. Jaderberg, M., Simonyan, K., Zisserman, A., Kavukcuoglu, K.: Spatial transformer networks. In: Conf. Neural Inf. Process. Syst. (NeurIPS). pp. 2017–2025 (2015)

18. Jaegle, A., Borgeaud, S., Alayrac, J.B., Doersch, C., Ionescu, C., Ding, D., Kop-pula, S., Zoran, D., Brock, A., Shelhamer, E., Hénaff, O., Botvinick, M.M., Zisser-man, A., Vinyals, O., Carreira, J.: Perceiver io: A general architecture for struc-tured inputs and outputs (2021)
19. Janai, J., Güney, F., Ranjan, A., Black, M., Geiger, A.: Unsupervised learning of multi-frame optical flow with occlusions. In: Eur. Conf. Comput. Vis. (ECCV) (September 2018)
20. Janai, J., Güney, F., Wulff, J., Black, M., Geiger, A.: Slow flow: Exploiting high-speed cameras for accurate and diverse optical flow reference data. In: IEEE Conf. Comput. Vis. Pattern Recog. (CVPR) (2017)
21. Jiang, S., Campbell, D., Lu, Y., Li, H., Hartley, R.: Learning to estimate hidden motions with global motion aggregation. In: Int. Conf. Comput. Vis. (ICCV) (2021)
22. Jonschkowski, R., Stone, A., Barron, J.T., Gordon, A., Konolige, K., Angelova, A.: What matters in unsupervised optical flow. In: Eur. Conf. Comput. Vis. (ECCV) (2020)
23. Kerl, C., Stücker, J., Cremers, D.: Dense continuous-time tracking and mapping with rolling shutter RGB-D cameras. In: Int. Conf. Comput. Vis. (ICCV) (2015). <https://doi.org/10.1109/ICCV.2015.261>
24. Lee, C., Kosta, A.K., Zhu, A.Z., Chaney, K., Daniilidis, K., Roy, K.: Spike-flownet: event-based optical flow estimation with energy-efficient hybrid neural networks. In: Eur. Conf. Comput. Vis. (ECCV) (2020)
25. Li, Z., Niklaus, S., Snavely, N., Wang, O.: Neural scene flow fields for space-time view synthesis of dynamic scenes. In: IEEE Conf. Comput. Vis. Pattern Recog. (CVPR) (2021). <https://doi.org/10.1109/cvpr46437.2021.00643>
26. Loshchilov, I., Hutter, F.: Decoupled weight decay regularization. In: Int. Conf. Learn. Representations (ICLR) (2019), <https://openreview.net/forum?id=Bkg6RiCqY7>
27. Lucas, B.D., Kanade, T.: An iterative image registration technique with an appli-cation to stereo vision. In: Int. Joint Conf. Artificial Intell. (IJCAI). pp. 674–679 (1981)
28. Maurer, D., Bruhn, A.: Proflow: Learning to predict optical flow. In: British Mach. Vis. Conf. (BMVC) (06 2018)
29. Mayer, N., Ilg, E., Häusser, P., Fischer, P., Cremers, D., Dosovitskiy, A., Brox, T.: A large dataset to train convolutional networks for dispar-ity, optical flow, and scene flow estimation. In: IEEE Conf. Comput. Vis. Pattern Recog. (CVPR) (2016), <http://lmb.informatik.uni-freiburg.de/Publications/2016/MIFDB16>, arXiv:1512.02134
30. Mueggler, E., Forster, C., Baumli, N., Gallego, G., Scaramuzza, D.: Lifetime esti-mation of events from dynamic vision sensors. In: IEEE Int. Conf. Robot. Autom. (ICRA). pp. 4874–4881 (2015). <https://doi.org/10.1109/ICRA.2015.7139876>
31. Mueggler, E., Gallego, G., Rebecq, H., Scaramuzza, D.: Continuous-time visual-inertial odometry for event cameras. IEEE Trans. Robot. **34**(6), 1425–1440 (Dec 2018). <https://doi.org/10.1109/tro.2018.2858287>
32. Niklaus, S., Liu, F.: Softmax splatting for video frame interpolation. In: IEEE Conf. Comput. Vis. Pattern Recog. (CVPR) (June 2020)
33. Pan, L., Liu, M., Hartley, R.: Single image optical flow estimation with an event camera. IEEE Conf. Comput. Vis. Pattern Recog. (CVPR) (2020)
34. Paredes-Vallés, F., de Croon, G.C.: Back to event basics: Self-supervised learning of image reconstruction for event cameras via photometric constancy. In: IEEE Conf. Comput. Vis. Pattern Recog. (CVPR) (2021)

35. Rebecq, H., Gehrig, D., Scaramuzza, D.: ESIM: an open event camera simulator. In: *Conf. on Robotics Learning (CoRL)* (2018)
36. Ren, Z., Gallo, O., Sun, D., Yang, M.H., Sudderth, E.B., Kautz, J.: A fusion approach for multi-frame optical flow estimation. In: *IEEE Winter Conf. Appl. Comput. Vis. (WACV)*. pp. 2077–2086 (2019). <https://doi.org/10.1109/WACV.2019.00225>
37. Ricco, S., Tomasi, C.: Dense lagrangian motion estimation with occlusions. In: *IEEE Conf. Comput. Vis. Pattern Recog. (CVPR)*. pp. 1800–1807 (2012). <https://doi.org/10.1109/CVPR.2012.6247877>
38. Seok, H., Lim, J.: Robust feature tracking in DVS event stream using bézier mapping. In: *IEEE Winter Conf. Appl. Comput. Vis. (WACV)* (2020). <https://doi.org/10.1109/wacv45572.2020.9093607>
39. Sun, D., Vlastic, D., Herrmann, C., Jampani, V., Krainin, M., Chang, H., Zabih, R., Freeman, W.T., Liu, C.: Autoflow: Learning a better training set for optical flow. In: *IEEE Conf. Comput. Vis. Pattern Recog. (CVPR)* (2021)
40. Sun, D., Yang, X., Liu, M.Y., Kautz, J.: PWC-Net: CNNs for optical flow using pyramid, warping, and cost volume. In: *IEEE Conf. Comput. Vis. Pattern Recog. (CVPR)* (2018)
41. Teed, Z., Deng, J.: Raft: Recurrent all-pairs field transforms for optical flow. In: *Eur. Conf. Comput. Vis. (ECCV)* (2020)
42. Tulyakov, S., Gehrig, D., Georgoulis, S., Erbach, J., Gehrig, M., Li, Y., Scaramuzza, D.: TimeLens: Event-based video frame interpolation. *IEEE Conf. Comput. Vis. Pattern Recog. (CVPR)* (2021)
43. Wulff, J., Black, M.J.: Efficient sparse-to-dense optical flow estimation using a learned basis and layers. In: *IEEE Conf. Comput. Vis. Pattern Recog. (CVPR)* (June 2015)
44. Xu, H., Yang, J., Cai, J., Zhang, J., Tong, X.: High-resolution optical flow from 1d attention and correlation. In: *Int. Conf. Comput. Vis. (ICCV)*. pp. 10498–10507 (October 2021)
45. Yang, G., Sun, D., Jampani, V., Vlastic, D., Cole, F., Liu, C., Ramanan, D.: ViSER: Video-specific surface embeddings for articulated 3d shape reconstruction. In: *Conf. Neural Inf. Process. Syst. (NeurIPS)* (2021)
46. Yang, G., Vo, M., Neverova, N., Ramanan, D., Vedaldi, A., Joo, H.: Banmo: Building animatable 3d neural models from many casual videos. *arXiv e-prints* (2022)
47. Ye, C., Mitrokhin, A., Fermüller, C., Yorke, J.A., Aloimonos, Y.: Unsupervised learning of dense optical flow, depth and egomotion with event-based sensors. In: *IEEE/RSJ Int. Conf. Intell. Robot. Syst. (IROS)* (2020)
48. Young, P., Lai, A., Hodosh, M., Hockenmaier, J.: From image descriptions to visual denotations: New similarity metrics for semantic inference over event descriptions. *Transactions of the Association for Computational Linguistics* (2014)
49. Zhang, F., Woodford, O.J., Prisacariu, V.A., Torr, P.H.: Separable flow: Learning motion cost volumes for optical flow estimation. In: *Int. Conf. Comput. Vis. (ICCV)*. pp. 10807–10817 (October 2021)
50. Zhao, S., Sheng, Y., Dong, Y., Chang, E.I., Xu, Y., et al.: Maskflownet: Asymmetric feature matching with learnable occlusion mask. In: *IEEE Conf. Comput. Vis. Pattern Recog. (CVPR)* (2020)
51. Zheng, Y., Zhang, M., Lu, F.: Optical flow in the dark. In: *IEEE Conf. Comput. Vis. Pattern Recog. (CVPR)* (June 2020)
52. Zhu, A.Z., Atanasov, N., Daniilidis, K.: Event-based feature tracking with probabilistic data association. In: *IEEE Int. Conf. Robot. Autom. (ICRA)* (2017). <https://doi.org/10.1109/icra.2017.7989517>

53. Zhu, A.Z., Yuan, L., Chaney, K., Daniilidis, K.: EV-FlowNet: Self-supervised optical flow estimation for event-based cameras. In: Robotics: Science and Systems (RSS) (2018). <https://doi.org/10.15607/RSS.2018.XIV.062>
54. Zhu, A.Z., Yuan, L., Chaney, K., Daniilidis, K.: Unsupervised event-based learning of optical flow, depth, and egomotion. In: IEEE Conf. Comput. Vis. Pattern Recog. (CVPR) (2019)